ISSN 1063-7745, Crystallography Reports, 2024, Vol. 69, No. 3, pp. 365–373. © Pleiades Publishing, Inc., 2024.

Chain-Melting Phase Transition in a Lamellar Film of Dimyristoyl-Phosphatidylserine on the Surface of a Silica Hydrosol

A. M. Tikhonov[a,*], Yu. O. Volkov[b], A. D. Nuzhdin[b], B. S. Roshchin[b], and V. E. Asadchikov[b]
[a] *Kapitza Institute for Physical Problems, Russian Academy of Sciences, Moscow, Russia*
[b] *National Research Centre "Kurchatov Institute," Moscow, Russia*
**e-mail: tikhonov@kapitza.ras.ru*

Received December 15, 2023; revised January 16, 2024; accepted January 23, 2024

Abstract—The structure dynamics in the temperature range of the melting phase transition of a dimyristoyl-phosphatidylserine multilayer on the surface of a colloidal silica solution with a particle diameter of 5 nm has been investigated by X-ray reflectometry and grazing diffraction of 71-keV photons. The joint model and model-free analysis of the reflectometry data revealed a structure consisting of a surface lipid monolayer and a set of lamellar bilayers sandwiched between water layers, with a period of ~150 Å. With an increase in temperature above the critical value one can observe a surface monolayer transition from a crystalline phase with a minimum area per lipid molecule of 40 ± 1 Å^2 to a disordered (liquid) phase with a calculated area per molecule of 52 ± 2 Å^2. At low temperatures, the data indicate that from five to eight H_2O molecules are tightly bound to the PS fragment of the lipid in both the monolayer and the bilayer structures. However, above the transition temperature, approximately 14 water molecules are attached to the headgroups of the bilayer: this is almost twice as many molecules as the eight H_2O molecules-per-headgroup in the surface monolayer.

DOI: 10.1134/S1063774524600509

INTRODUCTION

Biological membranes at the water–liquid interface play an important role in many cellular processes. Since a phospholipid bilayer is generally considered as a cell membrane model, its properties have been analyzed in many biophysical studies [1]. Monolayer and bilayer systems, consisting of lipids of different types, are of interest for biomedical research, because they imitate the surface of a natural membrane [2, 3]. One of unsolved problems in the field of interface phenomena is the exact characteristic of the phospholipid bilayer structure in an aqueous solution of electrolyte. This problem is complicated by the fact that the characteristic radius of spontaneous curvature of a phospholipid bilayer in an aqueous medium is less than 30 μm [4]. As a consequence, macroscopically flat samples for structural analysis are generally prepared either using the Langmuir–Blodgett method [5] or by depositing liposomes on different solid substrates [6, 7]. The first method, being relatively simple and inexpensive, allows one to form sufficiently flat extended lamellar films from Langmuir monolayers, formed initially at the air–water interface [8]. The second method does not make it possible to obtain homogeneous samples with sufficiently large geometric parameters, which is necessary, for example, for X-ray surface scattering experiments [9]. Thus, most studies devoted to the surface properties of phospholipids deal with either planar Langmuir monolayers [10] or solutions of single unilamellar vesicles and three-dimensional multilayer aggregates on solid substrates [11].

A new multilayer technology was described in [12]. It is based on spontaneous formation of a planar lamellar structure (for example, molecules of zwitterion phospholipid 1,2-distearoyl-*sn*-glycero-3-phosphocholine (DSPC)) on a polarized surface of silica hydrosol solution [13]. A specific feature of this system is the presence of a wide electrical double layer on the hydrosol surface [14]; the electric field of this layer orients dipole molecules of deposited lipid in it [15]. The thickness of the lipid film (i.e., the number of monolayers in it) can be controlled by changing the pH level in the hydrosol subphase [16]. This, relatively new method opens prospects for studying bilayer systems using surface-sensitive methods with a high spatial resolution, based on X-ray and neutron scattering [17, 18]. This method can also be useful for various applications related to multilayer amphiphilic thin films, for example, in nanotechnologies, for production of modern electron devices, or in optics; these issues are being widely discussed [19–21].

In this study we used synchrotron X-ray scattering to investigate the thermotropic dynamics of the structure of a hydrated lamellar multilayer of charged saturated phospholipid 1,2-dimyristoyl-*sn*-glycero-3-phospho-L-serine (DMPS) near the melting phase-transition temperature of hydrocarbon chains: $T_c \approx$ 36°C [22]. The system under consideration makes it

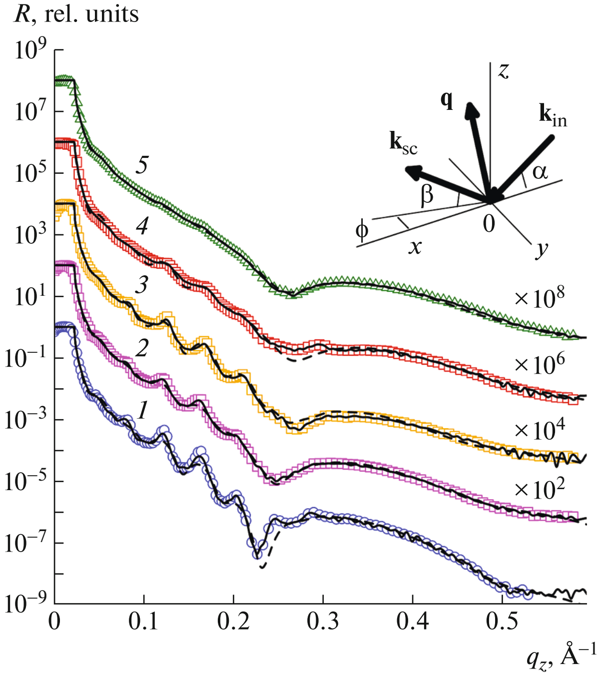

Fig. 1. X-ray reflectivity curves $R(q_z)$ for multilayer DMPS on the silica hydrosol surface with nanoparticles 5 nm in size. Curves *1–5* correspond to the data obtained at $T \approx 23$, 28, 34, 37, and 40°C, respectively. The solid and dotted lines show, respectively, the results of model-independent and model reconstructions. The inset presents the kinematics of X-ray scattering at the air–sol interface.

possible to investigate simultaneously and compare directly the thermotropic behavior of the monolayer and lipid bilayer in the same experiment. To reconstruct the depth profile of a DMPS film structure with a sufficiently high degree of reliability, an extended analysis of X-ray scattering data was performed based on the model-independent approach [23].

EXPERIMENTAL

Samples of DMPS phospholipid multilayers (Avanti Polar Lipids) were placed in a sealed one-stage thermostat with X-ray-transparent windows, which was described in [24]. Lipid films on the surface of colloidal silica, serving a substrate, were prepared in a Teflon plate 100 mm in diameter. A concentrated homogenized solution Ludox FM, stabilized by sodium hydroxide (Grace-Davison), contained silica particles ~50 Å in diameter (15 wt % SiO_2, pH ≈ 10). The Debye screening length in a silica suspension is $\Lambda_D = \sqrt{\varepsilon_0\varepsilon_1 k_B T/(c^- N_A e^2)} \approx 400$ Å, where ε_0 is the permittivity of free space, ε_1 is the permittivity of water, k_B is the Boltzmann constant, N_A is the Avogadro number, e is the elementary charge, and c^- is the volume concentration of OH^- (10^{-4} mol/L at pH =10).

To form a lipid film, a drop of 7 mL phospholipid solution (30 mg/mL in a mixture of chloroform and methanol 10 : 1) was deposited on the silica suspension surface using a Hamilton dosing syringe. The amount of material in this drop is sufficient to form a multilayer structure, consisting of approximately ten DMPS monolayers. Lipid spreading over meniscus was accompanied by a decrease in the surface tension γ at the air–hydrosol interface from the initial value of 74 mN/m to the final value of 35–40 mN/m. Then the lipid film was balanced in a thermostat at $T =$ 23°C for ~1 h.

The transverse and surface structures of DMPS multilayer at the air–hydrosol interface were investigated using, respectively, X-ray reflectivity and grazing incidence diffraction. Measurements were performed on the ID31 beamline of the European Synchrotron Radiation Facility (ESRF) (Grenoble, France) [25]. Experiments were carried out using a focused monochromatic beam with a photon energy ~71 keV ($\lambda = 0.1747 \pm 0.0003$ Å) and intensity up to 10^{10} photons/s. The transverse beam size was 250 × 10 μm. Data were collected using a CCD detector MaxiPix [26] (256 × 256 pixels, linear pixel size 55 μm).

Let us define $\mathbf{k}_{in}$ and $\mathbf{k}_{sc}$ as the wave vectors with an amplitude $k_0 = 2\pi/\lambda$ for the incident and scattered beams, respectively (Fig. 1). It is convenient to introduce a coordinate system in which the origin of coordinates O is located at the center of the illuminated region, the xy plane coincides with the air–sol interface, the x axis is oriented perpendicular to the beam direction, and the z axis passes along the normal to the surface in the direction opposite to the force gravity direction. We introduce also the following designations: α is the angle of incidence, β is the angle between the liquid surface plane and the direction to the detector in the plane of incidence yz, and ϕ is the angle between the incident ray direction and the scattering direction in the xy plane. Thus, the components of the scattering vector $\mathbf{q} = \mathbf{k}_{in} - \mathbf{k}_{sc}$ in the interface plane are, respectively, $q_z = k_0(\cos\beta\cos\phi - \cos\alpha)$ and $q_y = k_0\cos\alpha\sin\phi$, and its projection onto the z axis is $q_z = k_0(\sin\alpha + \sin\beta)$.

The X-ray reflectance was measured at $\beta = \alpha$ and $\phi = 0°$, so that $\mathbf{q}$ is directed exactly along the normal to the surface and $|\mathbf{q}| = q_z = 2k_0\sin\alpha$. The total external reflection angle for the air–sol interface is $\alpha_c = \lambda\sqrt{r_e\rho_b/\pi} \approx 1.8 \times 10^{-2\circ}$ ($q_c \approx 0.022$ Å^{-1}), where $r_e = 2.814 \times 10^{-5}$ Å is the electron Thomson scattering length. This angle is determined by the bulk density of hydrosol substrate electrons: $\rho_b \approx \rho_w$, where $\rho_w \approx 0.333$ e/Å^{-3} is the density of water electrons under normal conditions. The reflectance $R \approx 1$ at $q_z < q_c$.

Figure 1 shows the dependence $R(q_z)$ for the surfaces of hydrosol substrate with DMPS lipid films. Curves *1–5* were measured at temperatures $T \approx 23$, 28, 34, 37, and 40°C, respectively. With an increase in temperature the characteristic periodic peaks in the range of small q_z (curve *1* at $q_z < 0.3$ Å^{-1}) gradually smooth out and almost disappear at the highest temperature.

Figure 2 shows the total intensity of grazing-incidence diffraction $I_D(q_\parallel)$. This intensity is given as a function of the scattering vector component in the interface plane: $q_\parallel = (q_x^2 + q_y^2)^{1/2}$. Since $\alpha, \beta \ll 1$ in our experiment, $q_\parallel \approx (4\pi/\lambda)\sin(\phi/2)$. Diffraction data were obtained at the angle of incidence $\alpha \approx 8 \times 10^{-3\circ}$ and integrated over the angle β from 0° to 1° at $T = 23$ (circles) and 40°C (squares). This corresponds to the states of the lipid film before and after the melting phase transition, which occurs in the DMPS bulk at $T_c \approx 36$°C. Note that the diffraction peak intensity with respect to the specular reflection is very low (comparable with the level of scattering background noise in the experiment. The noise background was measured separately and then subtracted from the diffraction curve.

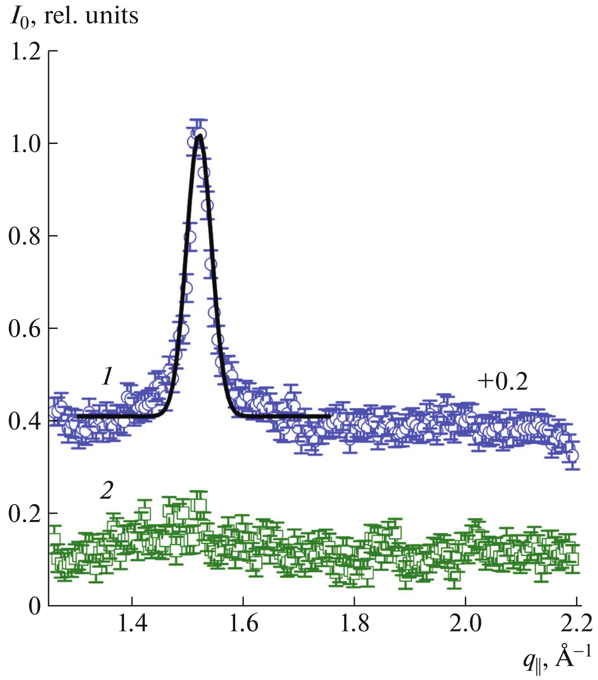

Fig. 2. Total grazing-incidence diffraction intensity $I_D(q_\parallel)$ from multilayer DMPS. Circles and squares present the data obtained at (*1*) 23 and (*2*) 40°C, respectively. The solid line illustrates fitting of the diffraction peak by the Gaussian function.

ANALYSIS OF X-RAY SCATTERING DATA

Specular Reflection

The experimental reflectivity and diffraction curves were averaged over the exposure region S with an area of ~0.5 cm^2. This circumstance makes it possible to consider the structure in the framework of a layered planarly inhomogeneous medium, on the assumption that the lateral correlation relief in the xy plane is independent of the electron density depth profile $\rho(z)$. To solve the inverse problem of X-ray reflectivity with a sufficiently high degree of reliability and obtain information about the interface structure along the normal to the surface, we applied the model-independent approach [27], which is based on the extrapolation of the asymptotic behavior of reflectance R at large wave vector values [23]. A significant difference of this approach from the conventional analysis based on structural models is that it does not require any a priori suggestions about the internal structure of the object. This approach was used previously to study the kinetics of formation of a similar lamellar structure in DSPC multilayers on the surface of a substrate from silica hydrosols [15].

Within the model-independent approach the only key assumption is that the distribution polarizability $\delta(z)$ contains a number of peculiar “discontinuity points,” at which the first derivative of the function $\delta(z) = \mathrm{Re}(1 - \varepsilon)$ (where ε is the permittivity in the X-ray spectrum) changes jumpwise: $\Delta(z_j) = d\delta(z_j + 0)/dz - d\delta(z_j - 0)/dz$, where z_j is the coordinate of the *j*th discontinuity point. The finite set of these points unambiguously determines the asymptotic behavior of the reflectivity curve, which in the case considered above corresponds to the Porod asymptotics: $R \propto (1/q)^4$ [28]. For the reflectivity curve $R(q_z)$, measured in a limited range of q_z, autocorrelations of polarizability depth distribution are estimated using the modified Fourier transform [23]

$$F(x) = \frac{16}{k_0^4(k_{\max} - k_{\min})} \int_{k_{\min}}^{k_{\max}} [k^4 R(k) - C]\cos(2kx)dk, \qquad (1)$$

$$C = \frac{1}{k_{\max} - k_{\min}} \int_{k_{\min}}^{k_{\max}} k^4 R(k)dk,$$

where $k = q_z/2$, and the range of integration from $k_{\min}$ to $k_{\max}$ is determined within the measured range of q_z. An analysis of the function $F(x)$ for different combinations of $k_{\min}$ and $k_{\max}$ values gives a set of stable extrema at fixed points $x = d_{ij}$, at which $F(d_{ij}) \approx \Delta(z_i)\Delta(z_j)$. In the general case, there are only two physically reasonable distributions $\delta(z)$, which satisfy the experimental curve $R(q_z)$, provide a specified set of singularities, and differ by only the sequence of location of these points along the z axis. The uniqueness of the solution to the inverse reflectometry problem, obtained by this method, was discussed in detail in [27].

Then the profile is parameterized by a Heaviside step function H(z) [29]. In this case, the structure is presented by a set ($M \approx 100$) of thin homogeneous

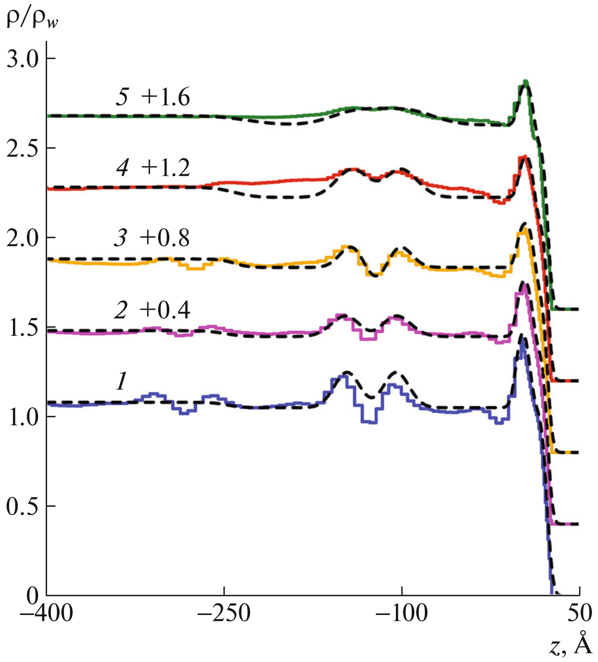

Fig. 3. Electron density profiles $\rho(z)$ calculated within the model-independent (solid lines) and model (dotted lines) approaches. Curves *1–5* correspond to the data obtained at $T \approx 23$, 28, 34, 37, and 40°C, respectively. For convenience, the curves are shifted along the ordinate axis. The values are normalized to the water electron density under normal conditions: $\rho_w = 0.333$ e/Å^{-3}.

cuts, so that $\delta(z) = \sum_{m=1}^{M} \Delta(z_m) H(z - z_m)$ with a fixed position of singularities z_j. Then the calculated reflectivity curve $R(q_z, \delta(z))$ is numerically fitted to the experimental data $R_{\exp}(q_z)$ using the polarizabilities of all layers in the distribution $\delta(z_1 \ldots z_M)$ as the optimization parameters [30]. Since the problem of numerical fitting is poorly caused in this case, to obtain a stable solution, we introduced an additional regularizing term $\sum_{m \neq j}^{M} (\delta_{m-1} - \delta_m) \to \min$, which provides smoothness of the desired distribution in the ranges between singularities. The standard Levenberg–Marquardt algorithm [31] was applied to search for a numerical solution. All calculations were implemented in the Python language using the Scientific Python package [32]. The polarizability profile $\delta(z)$ for a specific medium, obtained by this procedure, unambiguously determines the electron density depth profile $\rho(z) \approx 2\pi\delta(z)/r_0\lambda^2$ [33].

The solid lines in Fig. 1 are the fitting curves for specular reflection, calculated from the normalized electron density profile $\rho(z)/\rho_w$ (Fig. 3). It can be seen that the calculation results are in good agreement with the experimental data. The numbers of the curves in Figs. 1 and 3 correspond to the data obtained at $T \approx$ 23, 28, 34, 37, and 40°C.

Grazing-Incidence Diffraction

Curve *1* ($T < T_c$) in Fig. 2 exhibits a pronounced diffraction peak at $q_\parallel = 1.52$ Å^{-1}, which corresponds to an ordered molecular structure of DMPS. The solid line illustrates fitting of the diffraction peak by a Gaussian function with a half-width $\Delta q \approx 0.03$ Å^{-1}. Curve *2* in Fig. 2 shows flat scattering background at high temperatures $T > T_c$; the disappearance of the diffraction peak indicates structural surface disordering.

Under the grazing incidence conditions ($\alpha < 0.9\alpha_c$), the X-ray penetration depth into a material is approximately $\Lambda \approx \lambda/2\pi\alpha_c \approx 50$ Å; thus, nonspecular scattering occurs only from a thin surface layer. The grazing-incidence diffraction intensity I_D is determined by the equation

$$I_D \propto \int_S \langle \varepsilon(\mathbf{r}) - \varepsilon(\mathbf{r}') \rangle \exp(2i\pi \mathbf{q}_\parallel \mathbf{r})\, d\mathbf{r} \times \int_{-\infty}^{+\infty} \varepsilon(z) \exp(2iq_z z)\, dz, \qquad (2)$$

where $\mathbf{r} = (x, y)$ is the radius vector and S is the illuminated area. The presence of two-dimensional correlations in the surface plane leads to the occurrence of Bragg diffraction bands at $q = 2\pi/|\mathbf{h}|$, where $\mathbf{h}$ is the reciprocal lattice vector [34]. The second integral in Eq. (2) corresponds to the structure factor of the surface layer along the z axis.

Structural Model

Traditionally, hydrophobic and hydrophilic parts are selected in the phosphoglyceride DMPS molecule (Fig. 4). The hydrophobic part is formed by two aliphatic chains $-C_{13}H_{27}$ of the glycerol ethers of myristic acid in the positions C1 and C2. The hydrophilic part is formed by the polar glycerol-3-phospho-L-serine (PS) motif. The Na^+ cation in the phosphatidylserine membrane is located mainly near the phosphate group. The total number of electrons in the sodium salt $C_{34}H_{65}NO_{10}PNa$ is $\Gamma_h + \Gamma_t = 381$, where $\Gamma_h = 171$ and $\Gamma_t/2 = 105$ is the number of electrons in the PS-fragment with Na^+ and hydrocarbon tail $C_{13}H_{27}$, respectively. The total length of the DMPS molecule is ~25 Å.

The calculated electron density profile in Fig. 3 contains a feature in the form of a sharp peak at the air–lipid film interface, which corresponds to a layer of thickness $d \approx 30$ Å; this approximately corresponds to the thickness of a Langmuir DMPS monolayer [35]. The next feature is located at a distance $w \sim 100$ Å from the monolayer and has a width of $2d$, which presumably corresponds to a lipid bilayer. Therefore, it is expedient to continue the interpretation of Fig. 3 within the conventional model approach (see, e.g., [36]). In the first approximation it is suffi-

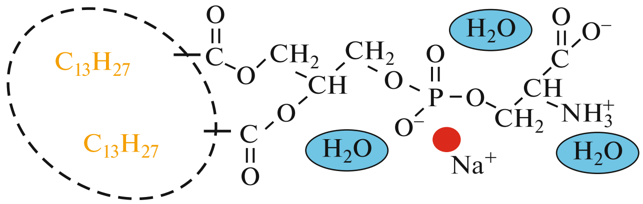

Fig. 4. Chemical structure of ionized DMPS molecule. The hydrophobic component is shown by a dotted line.

cient to restrict oneself to the layered model (Fig. 5) with four most pronounced structural elements, specifically, a DMPS monolayer and bilayer sandwiched between water layers with the density ~ρ_w. The model profile $\rho(z)$ corresponding to this structure has the form $\rho(z) \approx \rho_b/2 + P_1 + P_2$; it includes two structural components and the bulk component $\rho_b/2$.

The profile P_1, corresponding to the DMPS monolayer, is described by the equation

$$P_1(z) = \frac{1}{2}\sum_{j=0}^{2}(\rho_{j+1}-\rho_j)\,\mathrm{erf}\left(\frac{a_j(z)}{\sigma_0\sqrt{2}}\right),$$
$$a_j(z) = z - \sum_{n=0}^{j} L_n \qquad \mathrm{erf}(x) = \frac{2}{\sqrt{\pi}}\int_0^x e^{-y^2}dy \qquad (3)$$

with the following fitting parameters: $\rho_0 \approx \rho_w$ is the electron density of water layer, $L_0 \equiv 0$ is the position of the water–polar group interface ($z = 0$), and $\rho_3 = 0$ is the electron density of air. L_1 and L_2 are the thicknesses of the layers formed, respectively, by the head and acyl DMPS groups; ρ_1 and ρ_2 are the mean electron densities in the regions of head and acyl groups, respectively; and σ_0 is the surface roughness [37, 38]. The first, second, and third terms of the sum in Eq. (3) correspond, respectively, to the boundary between the surface of lipid head groups and the water substrate, the boundary between the regions of acyl and head groups, and the boundary between the environment and monolayer aliphatic tails.

One can suggest that the bilayer is located between electrolyte solution layers ("water" layers) and is formed by two lipid monolayers, oriented by aliphatic tails in a tail-to-tail way. Then the bilayer part of the P_2 profileis is determined by the following equation with six fitting parameters:

$$P_2(z) = \frac{1}{2}\sum_{j=0}^{4}(\zeta_{j+1}-\zeta_j)\,\mathrm{erf}\left(\frac{b_j(z)}{\sigma_{\mathrm{eff}}\sqrt{2}}\right),$$
$$b_j(z) = z + \sum_{n=0}^{j} l_n, \qquad (4)$$

where $l_0 = l_4 = w$, $l_1 = l_3$ (~ L_1), l_2 (~ $2L_2$) are, respectively, the thicknesses of the regions of head and acyl groups of the model bilayer; $\zeta_1 = \zeta_3$ and ζ_2 are the averaged electron densities of the regions formed by head and acyl groups, respectively; $\zeta_0 \equiv \zeta_4 \equiv \rho_0 \approx \rho_w$ and $\zeta_5 \equiv \rho_b$. As well as in Eq. (3), the terms of Eq. (4) describe the change in the electron density at four boundaries of the model bilayer, sandwiched between two water layers of thickness w.

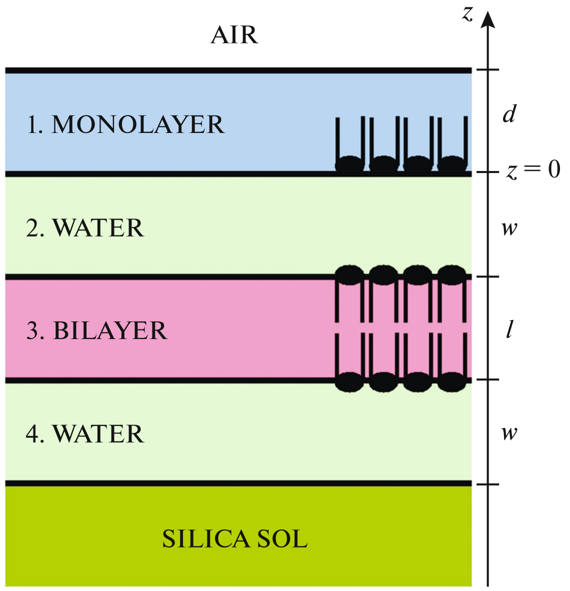

Fig. 5. Structural model of a multilayer DMPS film, constructed based on the analysis of model-independent calculations.

To estimate the fitting parameters, we used the first Born approximation, which relates the electron density gradient along the normal to the interface, averaged in the interface $\langle d\rho(z)/dz\rangle$, with the specular reflection as [39]

$$\frac{R(q_z)}{R_F(q_z)} \approx \left|\frac{1}{\rho_b}\int_{+\infty}^{-\infty}\left\langle\frac{d\rho(z)}{dz}\right\rangle \exp(iq_z z)\,dz\right|^2, \qquad (5)$$

where $R_F(q_z) \approx (q_z - [q_z^2 - q_c^2]^{1/2})^2/(q_z + [q_z^2 - q_c^2]^{1/2})^2$ is the Fresnel function.

The results of fitting reflectivity curves and model profiles are shown by dotted lines in Figs. 1 and 3, respectively. Only models with a minimum number of fitting parameters are presented. Within these models the "water" layer parameters (w, ρ_0) are practically the same for all fittings and estimated to be $w \approx 95$ Å and $\rho_0 \approx \rho_w$. The expected total thickness of model profiles is ~300 Å. At $T < T_c$ the experimental reflectivity curves are adequately described by the layered model with eight fitting parameters; within this model a bilayer consists of two surface tail-to-tail oriented monolayers ($l_1 = l_3 = L_1$, $\zeta_1 = \zeta_3 = \rho_1$, $l_2 = 2L_2$, $\zeta_2 = \rho_2$) and roughness parameter $\sigma_{\mathrm{eff}} \neq \sigma_0$. To describe experimental data at $T > T_c$, one needs another free fitting parameter ($\zeta_1 \neq \rho_1$). Estimates of the optimization

Table 1. Estimated parameters of a model DMPS monolayer according to (3)

T, °C	L_1, Å	L_2, Å	ρ_1/ρ_w	ρ_2/ρ_w	σ_0, Å	A, Å^2
23	11.6 ± 0.2	14.7 ± 0.2	1.53 ± 0.03	1.03 ± 0.03	3.8 ± 0.2	40 ± 1
28	13.4 ± 0.2	12.5 ± 0.2	1.38 ± 0.03	0.96 ± 0.03	3.4 ± 0.2	46 ± 1
34	14.7 ± 0.2	11.0 ± 0.2	1.29 ± 0.03	0.88 ± 0.03	3.4 ± 0.2	51 ± 2
37	12.8 ± 0.2	11.6 ± 0.2	1.27 ± 0.03	0.88 ± 0.03	3.2 ± 0.2	52 ± 2
40	12.8 ± 0.2	12.1 ± 0.2	1.28 ± 0.03	0.92 ± 0.03	3.3 ± 0.2	51 ± 2

L_1, L_2 are, respectively, the thicknesses of the head- and acyl-group regions and ρ_1, ρ_2 are, respectively, the averaged electron densities in the head- and acyl-group regions. The roughness σ_0 is the fitting parameter for the model monolayer. The electron densities are normalized to the water density under normal conditions: $\rho_w \approx 0.333$ e/Å^{-3}. A is the calculated area per lipid molecule in the surface monolayer.

Table 2. Estimated parameters of model DMPS bilayers according to (4)

T, °C	l, Å	w, Å	ζ_0/ρ_w	ζ_1/ρ_w	σ_{eff}, Å	$\Delta\Gamma/10$
23	53 ± 1	95 ± 3	1.05 ± 0.01	1.53 ± 0.03	10 ± 1	5 ± 1
28	52 ± 1	97 ± 3	1.05 ± 0.02	1.38 ± 0.03	12 ± 1	8 ± 1
34	51 ± 1	93 ± 3	1.03 ± 0.02	1.29 ± 0.03	10 ± 1	10 ± 1
37	49 ± 1	95 ± 3	1.02 ± 0.02	1.57 ± 0.03	14 ± 1	14 ± 1
40	50 ± 1	85 ± 5	1.01 ± 0.02	1.51 ± 0.03	19 ± 1	14 ± 1

The electron densities are normalized to the water density under normal conditions: $\rho_w \approx 0.333$ e/Å^{-3}. $\Delta\Gamma/10$ is the calculated number of H_2O molecules bound to the DMPS head group in the bilayer.

parameters of Eq. (3) for the monolayer and Eq. (4) for the bilayer are given in Tables 1 and 2, respectively. On the one hand, the quantitative model, which takes into account more than one lipid bilayer, is more consistent with the data obtained both at 23 and 28°C; however, it requires more fitting parameters, which inevitably leads to higher ambiguity of their estimates. At the same time, to solve the inverse reflectometry problem, the model approach based on volume limitations [40] is hardly applicable in this case because of the relatively narrow available range of q_z in the corresponding datasets.

RESULTS AND DISCUSSION

The calculated electron density depth profiles (Fig. 2) show the presence of a structure with a total thickness ranging from 500 to 300 Å (~Λ_D). This structure consists of a surface monolayer and a quasi-periodic lamellar component, where the distance between bilayers of polar DMPS molecules is ~100 Å. Similar structures were observed for films of zwitterion phosphocholines on the surface of silica sol solution [41]. The profiles indicate that the ordering of lipid layers is improved while approaching to the surface. A similar feature was described for other film structures, for example, liquid indium film [42], and for lamellar DSPC films [15]; however, significant differences were found for the films studied. First, the typical spontaneous ordering time τ for a DMPS film is less than 1 h, which is much smaller than the value τ ~ 24 h, observed previously for multilayers of zwitterion lipid DSPC [15]. Second, the characteristic structure period in the DMPS multilayer is ~150 Å, which is 3 times larger than the expected DMPS bilayer thickness, ~50 Å, as well as the periods of the lamellar structures formed by neutral phosphocholines: 60–70 Å [41].

Note that the monolayer thickness $d = L_1 + L_2$ is comparable with the radiation penetration depth Λ, in view of which only the upper monolayer structure was actually investigated in the grazing-incidence diffraction experiments. One pronounced diffraction peak in Fig. 2 at 1.52 Å^{-1} indicates that there is a high-symmetry hexagonal lattice of hydrocarbon lipid chains – $C_{13}H_{27}$ with a parameter $a = 4.8 \pm 0.1$ Å at the air–film interface in the low-temperature phase. This result corresponds to the maximum specific area per chain: $S_0 = 19.7 \pm 0.8$ Å^2; within the error, this value coincides with that for lamellar DMPS vesicles: $S_0 \approx 20.4$ Å^2 [11, 43, 44]. However, this value corresponds to somewhat smaller (by 5%) area per molecule, $A = 2S_0$, than in DSPC lipid monolayers (39.7 against 41.6 Å^2). This, relatively small area per molecule is nontrivial, because DMPS head groups, being charged, repulse from each other. It was suggested in [45] that the decrease in area per head group, for example, in bilayers of very similar compound—1,2-dipalmitoyl-*sn*-glycero-3-phosphoserine (DPPS)—is due to the strong intermolecular coordination between phosphoserine lipid molecules. This feature was discussed in detail in [43].

In the temperature range $T < T_c$, the two-layer model (Eq. (3)) efficiently describes this structural element with the parameters approximately equal to the parameters for the liquid crystal (LC) state of a Langmuir DMPS monolayer; these parameters were considered in detail in [46]. In particular, at the area per lipid $A \approx 41$ Å^2, it is assumed that approximately three water molecules are bound with the DMPS molecule. The calculated number of electrons in a model surface monolayer is $\Gamma = A(\rho_1 L_1 + \rho_2 L_2)$. Then the excess of electrons per a DMPS molecule in a monolayer can be estimated as $\Delta\Gamma = \Gamma - (\Gamma_h + \Gamma_t)$. This discrepancy in the electron density is due to the presence of additional hydrated water molecules and, possibly, some number of OH^- anions and Na^+ cations, penetrating the lipid film from the substrate bulk during film ordering. The transport and accumulation of these ions in the phospholipid film occurs presumably according to the electroporation mechanism, which was previously proposed to explain the equilibrium time in multilayer DSPC films [15, 47]. The total amount of stored material per lipid head group can be estimated as $\sim\Delta\Gamma/10$, taking into account that a Na^+ cation, H_2O molecule, and OH^- anion contain 10 electrons each. In a similar way one can estimate the degree of hydration of lipid molecules in a bilayer (Table 2). If we take into account that the ordering of a film with a PS fragment (for example, near the amino group) can be accompanied by binding up to one pair of ions (Na^+, OH^-) in addition to one sodium cation near the phosphate group, the number of water molecules bound with the lipid head in the monolayer (bilayer) reaches minimum: $\Delta\Gamma/10 = 2$.

With an increase in temperature the sharp features in $\rho(z)$ profiles, related to the lamellar structure presented in Fig. 3, gradually smooth out. At temperatures $T > T_c$ the feature related to the surface monolayer in Fig. 3 significantly attenuates. Above the melting transition point the peak in the grazing-incidence diffraction curve also disappears (Fig. 2), which is indicative of disordered (liquid) state of the monolayer. Using the density of acyl tails ρ_2 as the measure of their order, one can estimate the area per molecule in the model monolayer based on the molecular dynamics calculations for a liquid Langmuir monolayer [46], although these thermodynamic phases are radically different. For example, in the molten state at $T = 37°C$ $\rho_2 \approx 0.88\rho_w$ correspond to the monolayer area per molecule A equal to 52 ± 2 Å^2.

The values of the fitting roughness parameter σ_0 are consistent with the values given by the model of capillary-wave surface structure. In the experiment σ_0 was set by the short-wavelength limit $Q_{\max} = 2\pi/a$ and long-wavelength limit $Q_{\min} = q_z^{\max}\Delta\beta$ in the spectrum of capillary waves [38]:

$$\sigma_0^2 = \frac{k_B T}{2\pi\gamma}\ln\left[\frac{Q_{\max}}{Q_{\min}}\right], \quad (6)$$

where $a \approx 10$ Å is a parameter on the order of intermolecular distance and $2\Delta\beta \approx 0.04$ mrad is the detector angular resolution; $q_z^{\max} \approx 0.6$ Å^{-1}. For the surface tension $\gamma \approx 45$ mN/m Eq. (6) gives $\sigma_0 \approx 3.8$ Å, which is approximately equal to the fitting value at $T = 23°C$. According to Eq. (6), the decrease in the parameter σ_0 from 3.8 to 3.3 Å with an increase in temperature from 23 to 40°C may indicate an increase in the surface tension γ by ~10 mN/m.

Except for the effective roughness and integral density, the parameters for the model bilayer with the tail-to-tail configuration coincide with those for the monolayer in the entire range of measured temperatures (Table 2). The calculated bilayer thickness slightly decreases with an increase in temperature: from 53 ± 2 Å at 28°C to 49 ± 2 Å at 40°C. Estimates of $\Delta\Gamma/10$ show that, with an increase in temperature, the bilayer hydration increases by a factor of about 3: from 5 to 14 water molecules and ions per lipid molecule. Note that at temperatures above the T_c the degree of bilayer hydration is comparable with that for bulk hexagonal $P_{\beta'}$ and orthorhombic $L_{\beta'}$LC phases, for example, DPPC lipid [48]. In addition, at $T > T_c$ the ζ_1 value is so large ($\zeta_1 > \rho_1$) that the water content in the bilayer exceeds almost dpubles the calculated value: eight H_2O molecules per head group in the surface monolayer.

The effective roughness σ_{eff} varies from 10 to 20 Å in the measured temperature range; thus, it always significantly exceeds the contribution from the capillary-wave roughness σ_0. This effective roughness is generally related to the presence of internal structure of noncapillary-wave character, for example, because of the motion of SiO_2 nanoparticles from the substrate bulk to the surface and the corresponding violation of the bilayer planar structure. Apparently, melting of chains in the lipid film facilitates penetration of subphase nanoparticles into the surface structure, which may also facilitate both the transport of molten lipid material to the solution bulk (for example, due to the Brownian motion of particles) and their condensation on the hydrophilic surface of the surface monolayer [49].

It is convenient to compare the phase parameters in the presented thermodynamic system with the results of molecular dynamics (MD) simulation for bilayers of phosphoserine and phosphocholine lipids immersed in an electrolytic medium. According to the MD calculations [43] for a disordered phase, the area per head group in a DPPS bilayer (53.8 ± 0.1 Å^2) is 13% smaller than in the DPPC bilayer. A close value of 54 Å^2 per DPPS head group was obtained in [44]. These values are in fairly good agreement with the estimated area per molecule for a DMPS bilayer in the molten state, 52 ± 2 Å^2, and with the experimental values in the range of 45–55 Å^2, found for other systems [50, 51].

We did not investigate the reversibility of the melting transition in a lipid film, because such a study calls for very long-term measurements, which, in turn, are inconsistent with the limited time frame of the synchrotron experiment. However, we believe that the characteristic time of lipid film transformation from the molten state into ordered one may significantly exceed the initial formation time at temperatures below T_c (~1 h). The kinetics of this process can also be affected by the film radiative damage, which was studied in detail for Langmuir DMPS monolayers in [52].

CONCLUSIONS

The new technique for forming multilayers, combined with the methods of synchrotron X-ray reflectivity and grazing-incidence diffraction, was applied to study the structure and hydration of a macroscopically flat lamellar film of dimyristoyl derivative of PS in the range of melting phase transition at 36°C. Two mutually independent approaches were combined to solve the inverse problem of X-ray reflectivity with a sufficiently high degree of reliability and obtain information about the surface and transverse film structure at the interface. The first approach does not require any preliminary assumptions about the interface structure ("model-independent" approach), whereas the second one requires some a priori information about the possible structure of polar layers at the interface ("model" approach). The extended analysis of X-ray reflectivity data made it possible to reveal some specific features related to the layer-by-layer structure of DMPS film and explain these details by hydration and, to some expent, distribution of ion charges at the interfaces.

The model-independent reconstruction revealed a characteristic spatial period in the DMPS multilayer, which turned out to be ~150 Å. An analysis of the reconstruction shows that the bilayer is formed by two flat monolayers sandwiched between layers of water (electrolyte solution). Based on this result, we constructed a qualitative parametric structural model, consisting of lipid monolayers at the interface with air and tail-to-tail oriented bilayers between water layers of thickness ~100 Å; this model adequately describes the reflectometry data.

With an increase in temperature above T_c, a transition from the crystalline phase with an area per lipid of 40 ± 1 Å^2 to the disordered (liquid) phase with an estimated area per lipid of 52 ± 2 Å^2 occurs in the surface monolayer of thickness ~26 Å. The total estimated thickness of model bilayer is up to 51 ± 2 Å. At 23°C the calculated effective width of the water–bilayer–water interface is ~10 Å, which greatly exceeds the established value of 3.8 ± 0.2 Å for the width of the air–monolayer–water interface. In addition, at $T > T_c$ the former value increases to 20 Å, whereas the latter decreases to 3.3 ± 0.2 Å; these estimates (for the air–monolayer–water interface) lie in the range of roughnesses corresponding to surface capillary waves. The data obtained indicate that from three to five water molecules, both in the monolayer and bilayer, are closely bound to the PS fragment at low temperatures. However, at temperatures exceeding the melting transition point, up to 14 water molecules are bound to the bilayer head groups, which is almost twice as large as the number of molecules per head group (8) in the surface monolayer. The structural parameters of flat DMPS bilayers are in agreement with the previously published data, both the results of studying liposome solutions based on small-angle scattering and the MD calculation results.

ACKNOWLEDGMENTS

We are grateful to Dr. Veijo Honkimaki for assistance with experiments at ID31, Dr. Helena Isern and Florian Russello (ESRF) for help in the preparation of the experiments.

FUNDING

This work was performed within State assignments for the National Research Centre "Kurchatov Institute" and the Institute for Physical Problems of the Russian Academy of Sciences. The experiments on the synchrotron beamline ID31 were carried out within the project ESRF SC-4845.

CONFLICT OF INTEREST

The authors of this work declare that they have no conflicts of interest.

REFERENCES

1. D. M. Small, *The Physical Chemistry of Lipids.* (Plenum Press, New York, 1986).
2. H. Möhwald, *Handbook of Biological Physics,* Ed. by R. Lipowsky and E Sackmann. (Elsevier Science, Amsterdam, 1995), p. 161.
3. C. Stefaniu, G. Brezesinski, and H. Möhwald, Adv. Colloid Interface Sci. **208**, 197 (2014). https://doi.org/10.1016/j.cis.2014.02.013
4. D. Needham, T. J. McIntosh, and E. Evans, Biochemistry **27** (13), 4668 (1988). https://doi.org/10.1021/bi00413a013
5. K. B. Blodgett and I. Langmuir, Phys. Rev. **51** (11), 964 (1937). https://doi.org/10.1103/PhysRev.51.964
6. S. J. Johnson, T. M. Bayerl, D. C. McDermott, et al., Biophys. J **59** (2), 289 (1991). https://doi.org/10.1016/s0006-3495(91)82222-6
7. P. Théato and R. Zentel, Langmuir **16** (4), 1801 (2000). https://doi.org/10.1021/la990292l

8. J. K. Basu and M. K. Sanyal, Phys. Rep. **363** (1), 1 (2002). https://doi.org/10.1016/S0370-1573(01)00083-7
9. J. Koo, S. Park, S. Satija, et al., J. Colloid Interface Sci. **318** (1), 103 (2008). https://doi.org/10.1016/j.jcis.2007.09.079
10. V. M. Kaganer, H. Möhwald, and P. Dutta, Rev. Mod. Phys. **71** (3), 779 (1999). https://doi.org/10.1103/RevModPhys.71.779
11. N. Kucerka, Y. Liu, N. Chu, et al., Biophys. J. **88** (4), 2626 (2005). https://doi.org/10.1529/biophysj.104.056606
12. A. M. Tikhonov, JETP Lett. **92** (5), 356 (2010).
13. A. M. Tikhonov, J. Chem. Phys. **130** (2), 024512 (2009). https://doi.org/10.1063/1.3056663
14. A. M. Tikhonov, V. E. Asadchikov, Yu. O. Volkov, et al., J. Exp. Theor. Phys. **132** (1), 1 (2021).
15. A. M. Tikhonov, V. E. Asadchikov, Yu. O. Volkov, et al., JETP Lett. **104** (12), 873 (2016).
16. A. M. Tikhonov, V. E. Asadchikov, and Yu. O. Volkov, JETP Lett. **102** (7), 478 (2015).
17. C. A. Helm, P. Tippmann-Krayer, H. Möhwald, et al., Biophys. J. **60** (6), 1457 (1991). https://doi.org/10.1016/s0006-3495(91)82182-8
18. M. Delcea and C. A. Helm, Langmuir **35** (26), 8519 (2019). https://doi.org/10.1021/acs.langmuir.8b04315
19. X. Chen, S. Lenhert, M. Hirtz, et al., Acc. Chem. Res. **40** (6), 393 (2007). https://doi.org/10.1021/ar600019r
20. O. Purrucker, A. Förtig, K. Lüdtke, et al., J. Am. Chem. Soc. **127** (4), 1258 (2005). https://doi.org/10.1021/ja045713m
21. H. Kaur, S. Yadav, A. K. Srivastava, et al., Sci. Rep. **6**, 34095 (2016). https://doi.org/10.1038/srep34095
22. R. N. Lewis and R. N. McElhaney, Biophys. J. **79** (4), 2043 (2000). https://doi.org/10.1016/s0006-3495(00)76452-6
23. I. V. Kozhevnikov, Nucl. Instrum. Methods Phys. Res. A **508** (3), 519 (2003). https://doi.org/10.1016/S0168-9002(03)01512-2
24. A. M. Tikhonov, V. E. Asadchikov, Yu. O. Volkov, et al., Prib. Tekh. Eksp. **64** (1), 1 (2021). https://doi.org/10.1134/S0020441221010139
25. V. Honkimäki, H. Reichert, J. S. Okasinski, and H. Dosch, J. Synchrotron Rad. **13** (6), 426 (2006). https://doi.org/10.1107/s0909049506031438
26. C. Ponchut, J. M. Rigal, J. Clément, et al., J. Instrumentation **6**, C01069 (2011). https://doi.org/10.1088/1748-0221/6/01/C01069
27. I. V. Kozhevnikov, L. Peverini, and E. Ziegler, Phys. Rev. B **85** (12), 125439 (2012). https://doi.org/10.1103/PhysRevB.85.125439
28. P. Wong, Phys. Rev. B **32** (11), 7471 (1985). https://doi.org/10.1103/physrevb.32.7417
29. R. P. Kanwal, *Generalized Functions: Theory and Technique,* 2nd ed. (Birkhäuser Verlag, Boston, 1998).
30. L. G. Parratt, Phys. Rev. **95** (2), 359 (1954). https://doi.org/10.1103/PhysRev.95.359
31. J. Nocedal and S. Wright, *Numerical Optimizaton,* 2nd ed. (Springer, New York, 2006).
32. T. E. Oliphant, Comput. Sci. Eng. **9** (3), 10 (2007). https://doi.org/10.1109/MCSE.2007.58
33. B. L. Henke, E. M. Gullikson, and J. C. Davis, Atomic Data Nucl. Data Tables **54** (2), 181 (1993). https://doi.org/10.1006/adnd.1993.1013
34. J. Als-Nielsen, D. Jacquemain, K. Kjaer, et al., Phys. Rep. **246** (5), 251 (1994). https://doi.org/10.1016/0370-1573(94)90046-9
35. H. Möhwald, Annu. Rev. Phys. Chem. **41**, 441 (1990). https://doi.org/10.1146/annurev.pc.41.100190.002301
36. L. Hanley, Y. Choi, E. R. Fuoco, et al., Nucl. Instrum. Methods Phys. Res. B **203**, 116 (2003). https://doi.org/10.1016/S0168-583X(02)02183-3
37. F. P. Buff, R. A. Lovett, and F. H. Stillinger, Phys. Rev. Lett. **15** (15), 621 (1965). https://doi.org/10.1103/PhysRevLett.15.621
38. A. Braslau, M. Deutsch, P. S. Pershan, et al., Phys. Rev. Lett. **54** (2), 114 (1985). https://doi.org/10.1103/PhysRevLett.54.114
39. J. Als-Nielsen, J. Phys. B. Condens. Matter **61** (4), 411 (1985). https://doi.org/10.1007/BF01303545
40. M. Schalke and M. Lösche, Adv. Colloid Interface Sci. **88** (1–2), 243 (2000). https://doi.org/10.1016/s0001-8686(00)00047-6
41. A. M. Tikhonov, J. Exp. Theor. Phys. **131** (5), 714 (2020).
42. H. Tostmann, E. DiMasi, P. S. Pershan, et al., Phys. Rev. B **59** (2), 783 (1999). https://doi.org/10.1103/PhysRevB.59.783
43. S. A. Pandit and M. L. Berkowitz, Biophys. J. **82** (4), 1818 (2002). https://doi.org/10.1016/s0006-3495(02)75532-x
44. H. I. Petrache, S. Tristram-Nagle, K. Gawrisch, et al., Biophys. J. **86** (3), 1574 (2004). https://doi.org/10.1016/s0006-3495(04)74225-3
45. J. López Cascales, J. García de la Torre, S. J. Marrink, and H. J. Berendsen, J. Chem. Phys. **104** (7), 2713 (1996). https://doi.org/10.1063/1.470992
46. Y. A. Ermakov, V. E. Asadchikov, B. S. Roschin, et al., Langmuir **35** (38), 12326 (2019). https://doi.org/10.1021/acs.langmuir.9b01450
47. M. Tarek, Biophys. J. **88** (6), 4045 (2005). https://doi.org/10.1529/biophysj.104.050617
48. M. J. Ruocco and G. G. Shipley, Biochim. Biophys. Acta **691** (2), 309 (1982). https://doi.org/10.1016/0005-2736(82)90420-5
49. V. E. Asadchikov, V. V. Volkov, Yu. O. Volkov, et al., JETP Lett. **94** (7), 585 (2011).
50. G. Cevc, A. Watts, and D. Marsh, Biochemistry **20** (17), 4955 (1981). https://doi.org/10.1021/bi00520a023
51. R. A. Demel, F. Paltauf, and H. Hauser, Biochemistry **26** (26), 8659 (1987). https://doi.org/10.1021/bi00400a025
52. S. M. Danauskas, M. K. Ratajczak, Y. Ishitsuka, et al., Rev. Sci. Instrum. **78** (10), 103705 (2007). https://doi.org/10.1063/1.2796147

Translated by Yu. Sin'kov